POLITECNICO DI TORINO
Repository ISTITUZIONALE

An improved coupling of 3D state-based peridynamics with high-order 1D finite elements to reduce spurious effects at interfaces

Terms of use:

Publisher copyright

(Article begins on next page)

05 May 2024

RESEARCH ARTICLE

WILEY

An improved coupling of 3D state-based peridynamics with high-order 1D finite elements to reduce spurious effects at interfaces

F. Scabbia[1] | M. Enea[2]

[1]Center of Studies and Activities for Space (CISAS)–"G. Colombo", University of Padova, Padova, Italy

[2]MUL2 Group, Department of Mechanical and Aerospace Engineering, Politecnico di Torino, Torino, Italy

Correspondence

M. Enea, MUL2 Group, Department of Mechanical and Aerospace Engineering, Politecnico di Torino, Corso Duca degli Abruzzi 24, 10129 Torino, Italy.
Email: marco.enea@polito.it

Abstract

Peridynamics (PD) is a nonlocal continuum theory capable of handling fracture mechanisms with ease. However, its use involves high computational costs. On the other hand, Carrera Unified Formulation (CUF) allows one to use one-dimensional high-order finite elements, resulting in excellent accuracy while improving computational efficiency. To address the high computational cost of solving fracture problems, a coupling technique between these two theories is necessary. Various approaches have been proposed to couple peridynamic grids with finite element meshes in the literature. However, most of these approaches are affected by arbitrary choices of blending functions and tuning parameters or exhibit spurious effects at the interfaces. To overcome these issues, we propose a simple coupling technique based on overlapping PD/CUF regions and continuity of the displacement field at the interfaces. This approach is verified through static analysis of classical beams and thin-walled structures with applications in the aerospace industry.

KEYWORDS

coupling, finite element method, higher-order elements, peridynamics

1 | INTRODUCTION

Peridynamic (PD) theory has been introduced for the first time by Silling in Reference 1. This first formulation of the theory was named bond-based peridynamics (BB-PD) and has the limitation that the Poisson's ratio value is fixed (for instance, $\nu = 0.25$ in 3D models). A more general formulation of the theory that overcomes this restriction, namely the state-based peridynamics (SB-PD), has been proposed in Reference 2. The main idea of the peridynamic theory relies on the fact that two PD points in a solid body interact with each other when their distance is lower than the horizon radius, called δ. Thus, PD is a nonlocal theory, and it is based on integro-differential equations. For this reason, PD has been widely used for dealing with discontinuous displacement fields, such as those in fracture mechanic problems,[3,4] due to the possibility of avoiding the shortcomings of classical continuum mechanics.

However, it should be highlighted that the nonlocal nature of PD theory leads to higher computational analysis costs if compared with those from classical computational methods, that is, finite element method (FEM). Indeed, PD leads

F. Scabbia and M. Enea contributed equally to this article.

to solving systems with sparse, large, and not banded matrices, making the solution of fully 3D problems of practical engineering interest impossible. Furthermore, the handling of the nonlocal boundaries requires specific methods, such as, for example, References 5-8, to reduce the PD surface effect, that is, an undesired stiffness fluctuation near the external surface of the body, and to impose the boundary conditions. If FEM is used at the external boundary of the body, these problems are avoided altogether.

On these bases, researches are now focused on providing coupling strategies between FEM models and PD domains in order to exploit the advantages of both numerical methods and adopt PD in relatively small regions of interest. Kilic and Madenci[9] propose a coupled method where an overlap region is identified. In this region, both peridynamic and finite element equations are used at the same time. In Reference 10 and 11, a progressive morphing between local and nonlocal interactions is adopted. A transition affecting only the constitutive parameters is employed to perform the coupling strategy. Seleson and co-workers[12,13] propose a strong coupling between local and nonlocal approaches for integrated fracture modeling. In Reference 14, the coupling is achieved by the introduction of the partial stress concept for the connection of nonlocal models with different horizon radius. Sun and Fish[15] introduced a superposition-based coupling model between bond-based PD and FEM. A partial superposition of nonlocal (PD) and local (FEM) solution is considered. The continuity of the solution is achieved by imposing appropriate homogeneous boundary conditions. Galvanetto and his co-workers[16,17] propose a coupling strategy based on the adaptive transformation of FEM nodes into PD particles, which has shown to be effective for static, dynamic, and fracture problems and from one-dimensional to three-dimensional models.[16-21]

It should be underlined that most of the aforementioned methods are able to couple FEM and PD domains of consistent dimensions. However, some particular situations may need the adoption of 3D peridynamics domains in local zones of the structure. In this case, the coupling of 3D FEM with 3D PD models may be unfeasible, due to the consequent huge computational cost. An example of a coupling method between refined 1D models and a 3D bond-based perydinamic grid is provided in Reference 22. The 1D models are based on the Carrera Unified Formulation (CUF), whose governing equations are formulated in terms of fundamental nuclei, which are invariant with the theory approximation order. The coupling is realized through the adoption of Lagrange multipliers,[23-25] which are applied at the interface between the two domains in order to assure continuity. This technique demonstrates to be general and consistent, due to the fact that Lagrange multipliers have a clear physical meaning. Results show that this method allows to obtain 3D-like accuracy solutions by adopting a one-dimensional refined model and 3D Peridynamic, thus reducing the computational cost. Moreover, the use of Lagrange multipliers allows the possibility of introducing 3D PD regions only in zones of interest, which can also be embedded into the FE domain. Nevertheless, some numerical distortions are detected at the FE-PD interface, requiring some artificial expedient (i.e., overlapping region) to eliminate these errors.

In this work, the authors propose a different coupling method, which can fully exploit the CUF formulation's potentiality in combination with the 3D peridynamics domain and greatly reduce numerical error at the interface between two different domains.[26] This method is based on the continuity of the displacement field at the interface.[16,19] The forces acting at the interface are provided by introducing fictitious nodes beyond the interface itself: a fictitious FEM node is added in the PD region, and some fictitious PD nodes are added in the FEM region. The coupling is then achieved by considering that peridynamic forces are exerted only on PD nodes, while finite elements apply forces only on FE nodes. The effectiveness of this strategy has already been proven when applied to couple classical FE elements with PD domains.[16,17,19] Thanks to this improved coupling approach, the spurious effects that were present at the interfaces in Reference 22 can be considerably reduced. Moreover, for the first time state-based peridynamics has been coupled with CUF formulation, which allows the model to have no restrictions on the value of the Poisson's ratio. The article is organized as follows: Section 2 explains the basis of the state-based peridynamics formulation; high-order one-dimensional CUF-based elements are discussed in Section 3; then, the proposed coupling approach is described in Section 4; some numerical results, such as thin-walled beams and a reinforced aeronautical panel, are discussed in Section 5; finally, the main conclusions are drawn in Section 6.

2 | STATE-BASED PERIDYNAMICS

The first formulation of the peridynamic theory, named bond-based Peridynamics,[1] has been extensively exploited for its simplicity of implementation. However, due to the assumptions of this formulation, the Poisson's ratio is constrained to $\nu = 0.25$ in 3D bodies. To overcome this limitation, the state-based formulation of the theory was introduced in Reference 2. The state-based peridynamics is used in this work.

2.1 | Continuum formulation

Two peridynamic points, for instance $\mathbf{x}$ and $\mathbf{x}'$ shown in Figure 1, interact through a *bond* that is identified by their relative position vector

$$\xi = \mathbf{x}' - \mathbf{x}. \tag{1}$$

This interaction vanishes if the distance between the interacting points exceeds the value δ, which is called *horizon size*. Therefore, a peridynamic point interacts with all the points within a sphere centered in that point and with a radius equal to δ. The set of the points within this sphere is named *neighborhood* and denoted by $\mathcal{H}$. In the deformed configuration, the relative displacement vector η is defined as

$$\eta = \mathbf{u}(\mathbf{x}', t) - \mathbf{u}(\mathbf{x}, t), \tag{2}$$

where $\mathbf{u}$ is the displacement field. Note that the relative position vector at instant t between points $\mathbf{x}$ and $\mathbf{x}'$ is given by $\xi + \eta$.

The peridynamic equation of motion of point $\mathbf{x}$ is given by Silling et al.[2]

$$\rho(\mathbf{x})\,\ddot{\mathbf{u}}(\mathbf{x}, t) = \int_{\mathcal{H}_{\mathbf{x}}} \left(\underline{\mathbf{T}}[\mathbf{x}, t]\langle \xi \rangle - \underline{\mathbf{T}}[\mathbf{x}', t]\langle -\xi \rangle\right) dV_{\mathbf{x}'} + \mathbf{b}(\mathbf{x}, t), \tag{3}$$

where ρ is the material density, $\ddot{\mathbf{u}}$ is the acceleration field, $\underline{\mathbf{T}}$ is the force density vector state (force per unit volume squared), $dV_{\mathbf{x}'}$ is the differential volume of a point $\mathbf{x}'$ within the neighborhood $\mathcal{H}_{\mathbf{x}}$ and $\mathbf{b}$ is the external body force density field. The notation $\underline{\mathbf{T}}[\mathbf{x}, t]\langle \xi \rangle$ means that the force density scalar state $\underline{\mathbf{T}}$ depends on point $\mathbf{x}$ and instant t and is applied to the bond vector ξ. In quasi-static conditions, the equilibrium equation of point $\mathbf{x}$ is given as

$$-\int_{\mathcal{H}_{\mathbf{x}}} \left(\underline{\mathbf{T}}[\mathbf{x}]\langle \xi \rangle - \underline{\mathbf{T}}[\mathbf{x}']\langle -\xi \rangle\right) dV_{\mathbf{x}'} = \mathbf{b}(\mathbf{x}). \tag{4}$$

Note that $\underline{\mathbf{T}}[\mathbf{x}]\langle \xi \rangle$ and $\underline{\mathbf{T}}[\mathbf{x}']\langle -\xi \rangle$ must have the same magnitude in bond-based peridynamics, whereas may have different magnitudes in state-based peridynamics (see Figure 1).

In the following, we define some quantities that will be useful to compute the force density vector state $\underline{\mathbf{T}}[\mathbf{x}]\langle \xi \rangle$. The reference position scalar state $\underline{x}$, which represents the bond length in the initial configuration, and the extension scalar state $\underline{e}$, which represents the elongation (or contraction) of the bond in the deformed configuration, are defined respectively as

$$\underline{x}\langle \xi \rangle = \|\xi\|, \tag{5}$$

$$\underline{e}\langle \xi \rangle = \|\xi + \eta\| - \|\xi\|. \tag{6}$$
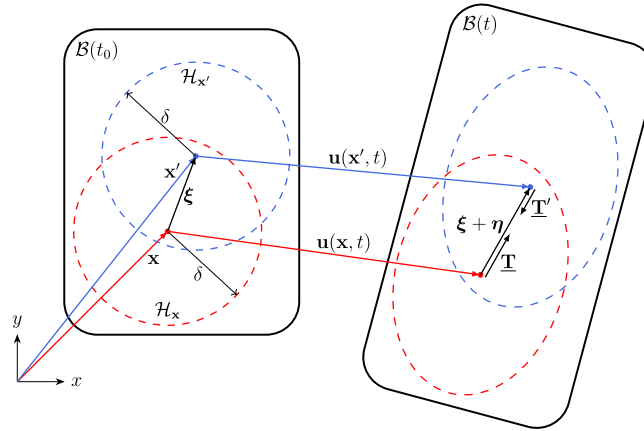
FIGURE 1 Reference configuration of the body $\mathcal{B}$ at instant t_0 (on the left) and deformed configuration at instant t (on the right). When the bond ξ between points $\mathbf{x}$ and $\mathbf{x}'$ is deformed, the force density vector states $\underline{\mathbf{T}} = \underline{\mathbf{T}}[\mathbf{x}, t]\langle \xi \rangle$ and $\underline{\mathbf{T}}' = \underline{\mathbf{T}}[\mathbf{x}', t]\langle -\xi \rangle$ arise within the bond.

On the other hand, the weighted volume m and the dilatation θ of a point $\mathbf{x}$ are defined respectively as

$$m(\mathbf{x}) = \int_{\mathcal{H}_\mathbf{x}} \underline{\omega}\, \underline{x}^2 \mathrm{d}V_{\mathbf{x}'},$$
(7)

$$\theta(\mathbf{x}) = \frac{3}{m(\mathbf{x})} \int_{\mathcal{H}_\mathbf{x}} \underline{\omega}\, \underline{x}\, \underline{e} \mathrm{d}V_{\mathbf{x}'},$$
(8)

where $\underline{\omega}$ is a prescribed spherical influence function. We adopt in this work the Gaussian influence function:

$$\underline{\omega} = \exp\left(-\frac{\|\xi\|^2}{\delta^2}\right).$$
(9)

In ordinary state-based peridynamics, the force density vector state is aligned with the deformed direction vector state (unit vector in the direction of the corresponding bond):

$$\underline{\mathbf{M}}\langle\xi\rangle = \frac{\xi + \eta}{\|\xi + \eta\|}.$$
(10)

Therefore, adopting the linear peridynamic solid model,[2] the force density vector state is computed as

$$\underline{\mathbf{T}}[\mathbf{x}]\langle\xi\rangle = \frac{\underline{\omega}\langle\xi\rangle}{m(\mathbf{x})} \left[(3K - 5\mu)\, \theta(\mathbf{x})\, \underline{x}\langle\xi\rangle + 15\mu\, \underline{e}\langle\xi\rangle\right] \underline{\mathbf{M}}\langle\xi\rangle,$$
(11)

where K is the bulk modulus and μ is the shear modulus.

2.2 | Discretization

The peridynamic body is discretized by the meshfree method with a uniform grid spacing h, which is arguably the most commonly used method.[27-29] Each node represents a cell with a volume $V = h^3$. Consider a node i and its neighborhood $\mathcal{H}_i$, as shown in Figure 2. We define as β, called *quadrature coefficient*, the fraction of volume cell that lies within $\mathcal{H}_i$. The value of the quadrature coefficient β is comprised between the extreme values 0 (if the cell is completely outside $\mathcal{H}_i$) and 1 (if the cell is completely outside $\mathcal{H}_i$). Clearly, a node is considered part of the neighborhood only if the quadrature coefficient of its cell is $\beta > 0$. The computation of the quadrature coefficients in 3D peridynamics can be carried out in several ways (see, for instance, References 29-31). For simplicity, we adopt the method illustrated in Reference 32 for this work.

The relative position vector of the bond ij that connects nodes i and j can be computed as

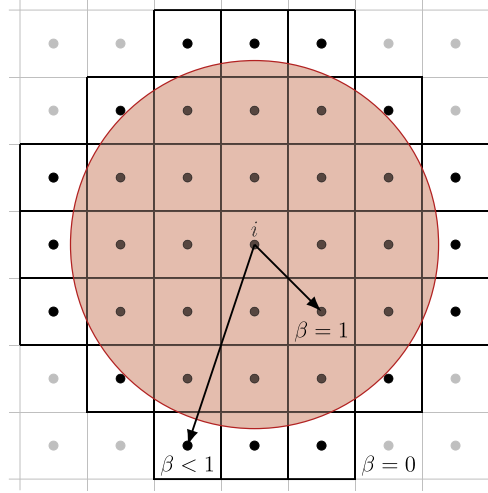$$\xi_{ij} = \mathbf{x}_j - \mathbf{x}_i,$$
(12)

where $\mathbf{x}_i$ and $\mathbf{x}_j$ are the position vectors of the two nodes. Similarly, the relative displacement vector of the bond is evaluated as

$$\eta_{ij} = \mathbf{u}_j^{PD} - \mathbf{u}_i^{PD},$$
(13)

where $\mathbf{u}_i^{PD}$ and $\mathbf{u}_j^{PD}$ are the displacement vectors of the peridynamic nodes. The reference position scalar state and the influence function of the bond are computed as

$$\underline{x}_{ij} = \|\xi_{ij}\|,$$
(14)

$$\underline{\omega}_{ij} = \exp\left(-\frac{\|\xi_{ij}\|^2}{\delta^2}\right).$$
(15)

FIGURE 2 The neighborhood $\mathcal{H}_i$ of a node i consists of the nodes with $\beta > 0$, where β is the quadrature coefficient computed as the fraction of the cell volume lying within the neighborhood.

Under the assumption of small displacements ($\|\boldsymbol{\eta}_{ij}\| \ll \|\boldsymbol{\xi}_{ij}\|$), the deformed direction vector state and the extension scalar state are respectively given as

$$\underline{\mathbf{M}}_{ij} = \frac{\boldsymbol{\xi}_{ij} + \boldsymbol{\eta}_{ij}}{\|\boldsymbol{\xi}_{ij} + \boldsymbol{\eta}_{ij}\|} \approx \frac{\boldsymbol{\xi}_{ij}}{\|\boldsymbol{\xi}_{ij}\|}, \tag{16}$$

$$\underline{e}_{ij} = \|\boldsymbol{\xi}_{ij} + \boldsymbol{\eta}_{ij}\| - \|\boldsymbol{\xi}_{ij}\| \approx \boldsymbol{\eta}_{ij} \cdot \underline{\mathbf{M}}_{ij}. \tag{17}$$

In the discretized model, the integrals over a neighborhood are numerically computed as the summation of the integrand evaluated for each node contained in that neighborhood. Therefore, the weighted volume m and the dilatation θ of a node i are given as

$$m_i = \sum_{j \in \mathcal{H}_i} \underline{\omega}_{ij} \, \underline{x}_{ij}^2 \, \beta_{ij} V, \tag{18}$$

$$\theta_i = \frac{3}{m_i} \sum_{j \in \mathcal{H}_i} \underline{\omega}_{ij} \, \underline{x}_{ij} \, \underline{e}_{ij} \, \beta_{ij} V, \tag{19}$$

where β_{ij} is the quadrature coefficient of the bond ij and V is the volume of the cell of node j. Therefore, the force density vector state is computed as

$$\underline{\mathbf{T}}_{ij} = \frac{\underline{\omega}_{ij}}{m_i} \left[(3K - 5\mu) \, \theta_i \, \underline{x}_{ij} + 15\mu \, \underline{e}_{ij} \right] \underline{\mathbf{M}}_{ij}. \tag{20}$$

Now, we can write the equilibrium equation of a node i in the discretized form (multiplying both sides of the equation by the cell volume $V_i = V$) as follows:

$$-\sum_{j \in \mathcal{H}_i} \left(\underline{\mathbf{T}}_{ij} - \underline{\mathbf{T}}_{ji} \right) \beta_{ij} V^2 = \mathbf{b}_i \, V, \tag{21}$$

where $\mathbf{b}_i$ is the external force density vector applied to node i. Equation (21) can be rewritten in the standard form

$$\mathbf{K}^{PD} \mathbf{U}^{PD} = \mathbf{F}^{PD}, \tag{22}$$

where $\mathbf{K}^{PD}$ is the peridynamic stiffness matrix, $\mathbf{U}^{PD}$ is the peridynamic displacement vector and $\mathbf{F}^{PD}$ is the peridynamic force vector.

3 | HIGH ORDER 1D FINITE ELEMENTS

The major shortcoming of the perdynamic theory is that the resulting stiffness matrix is sparse and generally not banded. Furthermore, the nonlocal nature of this method makes the computational costs arise exponentially. Therefore, researchers are working on coupling peridynamics with finite elements. In this work, 3D PD domains are coupled with 1D FEs, based on the Carrera Unified Formulation (CUF). This formulation is known in the literature as capable of generating high-order theories with great accuracy and considerably reducing the overall computational weight.[33]

3.1 | The Carrera unified formulation

Let's consider a generic beam structure aligned along the y-axis and measuring l in length and Ω in cross-section. In this formulation, the cross-sectional shape of the beam has no influence on its validity. In the CUF's framework, the 3D displacement field of this beam can be formulated as follows:

$$\mathbf{u}(x, y, z) = F_\tau(x, z)\mathbf{u}_\tau(y), \qquad \tau = 1, 2, \dots, M, \tag{23}$$

where $\mathbf{u}(x, y, z)$ is the displacement vector; F_τ are the cross-section expansion functions; $\mathbf{u}_\tau$ is the generalized displacement vector; M is the number of terms in the expansion. The subscript τ indicates summation. In addition, F_τ and M may be freely chosen. Based on the selected expansion functions, the class of the 1D CUF model is determined. A first example is denoted by the Taylor expansion (TE) models, which have been widely employed in CUF's framework, as in References 34 and 35. In the case of TE models, Mclaurin polynomials of truncated order N are employed to expand the generalized displacements $\mathbf{u}_\tau$ around the beam axis. TE models could be very efficient for different problems. However, some errors can be detected if complex structures are investigated. In order to solve these kinds of problems, Lagrange expansion (LE) models are employed. In this case, Lagrange-like polynomials are used to expand the generalized displacements around the beam axis. The most important feature of LE models is that they make use of local expansions of pure displacement variables. The main advantage is that LE models allow a more refined discretization in specific regions of interest, leading to a higher solution accuracy. Furthermore, LE models enables to reproduce 3D-like solutions at a global-local scale.

3.2 | Finite element approximation

Using 1D finite elements, the generalized displacement $\mathbf{u}_\tau$ is approximated along the beam axis:

$$\mathbf{u}_\tau(y) = N_i(y)\, \mathbf{u}_{\tau i}, \qquad i = 1, 2, \dots, p + 1 \tag{24}$$

where p is the number of nodes for each element. In Equation (24), the index i means summation. The generalized displacements are expressed as a function of the unknown nodal vector, $\mathbf{u}_{\tau i}$, and the 1D shape functions, N_i. Note that Equation (24) does not depend on the adopted refined 1D theory.

The governing equations are written using the principle of virtual work. For linear static problems, it is formulated in the following way:

$$\delta L_{\text{int}} = \delta L_{\text{ext}} \tag{25}$$

where δ is the virtual variation, L_{int} the work of the internal strain energy, and L_{ext} the work of the external forces. The internal work expression reads as:

$$\delta L_{\text{int}} = \int_l \int_\Omega \delta \boldsymbol{\epsilon}^T \boldsymbol{\sigma} \, d\Omega \, dy \tag{26}$$

where σ and ϵ are the vectors of 3D stresses and strains. By replacing the constitutive and geometric equations along with Equations (23) and (24), the internal work formula can be reformulated as follows:

$$\delta L_{\text{int}} = \delta \mathbf{u}_{sj}^T \mathbf{K}^{\tau sij} \mathbf{u}_{\tau i} \tag{27}$$

where $\mathbf{K}^{\tau sij}$ is the 3×3 fundamental nucleus of the element stiffness matrix of the refined 1D beam theory. Using the four indexes τ, s, i, and j, the fundamental nucleus can be expanded to form any refined beam model. Then, after expansion of the stiffness matrix and after assembly over the whole domain, Equation (25) is written as follows:

$$\mathbf{K}^{FE}\mathbf{U}^{FE} = \mathbf{F}^{FE}, \tag{28}$$

where $\mathbf{K}^{FE}$ is the stiffness matrix, $\mathbf{U}^{FE}$ is the vector of the FE nodal unknowns and $\mathbf{F}^{FE}$ is the vector of external forces.

4 | IMPROVED COUPLING

Given its high computational cost, peridynamics is preferably used only in regions where cracks are likely to propagate, whereas the rest of the body can be modeled by methods derived from classical continuum mechanics, such as the Carrera Unified Formulation (CUF). The coupling of high-order 1D FEs with a peridynamic grid of nodes has already been achieved via the use of Lagrange multipliers.[22,36] However, the numerical solution obtained with this method exhibits undesired fluctuations of the solution near the interfaces.

An improved method to couple finite element method (FEM) and peridynamics (PD) has been developed in References 16-20. This method, based on the continuity of the displacement field at the interfaces, is reviewed in the following subsection. Inspired by that, we develop a method to couple high-order 1D FEs and PD nodes.

4.1 | 1D coupling of FEs and PD nodes

Consider a 1D body, in which a region is discretized with 1D FEs and another region with equispaced PD nodes, as shown in Figure 3. Each PD node represents a portion of the 1D body of length Δx and is positioned at the center of this portion. Therefore, the PD node closest to the interface is distant $\Delta x/2$ from the interface itself, as shown in Figure 3A. On the other hand, the closest FEM node lies exactly at the interface. For simplicity, the length $\Delta \ell$ of the FEs is considered to be constant. The length $\Delta \ell$ of the FEs and the PD spacing Δx are not necessarily equal to each other.

The improved coupling method is based on the continuity of the displacement field at the interface.[16,19] The forces acting at the interface are provided by the introduction of fictitious nodes beyond the interface itself: a fictitious FEM node is added in the PD region and some fictitious PD nodes are added in the FEM region.

On the one hand, the new fictitious FEM node is positioned, for simplicity, at a distance $\Delta \ell$ from the interface, as shown in Figure 3B. Its displacement is determined by interpolation of the displacements of the real PD nodes surrounding it. Since the fictitious FEM node lies in the PD region and cannot "feel" FEM forces, it is not subjected to the force of the fictitious FE. However, that force is applied to the real FEM node at the interface. Note that, due to the displacement interpolation, the force of the fictitious FE depends on the displacements of the real PD nodes.

On the other hand, some fictitious PD nodes are introduced in the FEM region to complete the neighborhoods of the real PD nodes near the interface, as shown in Figure 3C. The displacements of the fictitious PD nodes can be determined by means of an interpolation of the real FEM nodes. The forces of the fictitious bonds, that is, the bonds crossing the interface, are applied only to the real PD nodes because the fictitious PD nodes lie in the FEM region. Note that, due to the displacement interpolation, the forces of the fictitious bonds depends on the displacements of the real FEM nodes.

In the case of a linear displacement field, the force applied to the FEM node at the interface through the fictitious FE (see Figure 3B) is equal to the sum of the forces applied to the real PD nodes through the fictitious bonds (see Figure 3C).[26] The concepts of this improved coupling method are hereinafter extended to couple a 3D peridynamic grid with high-order 1D elements (or CUF elements), as shown, for instance, in Figure 4.
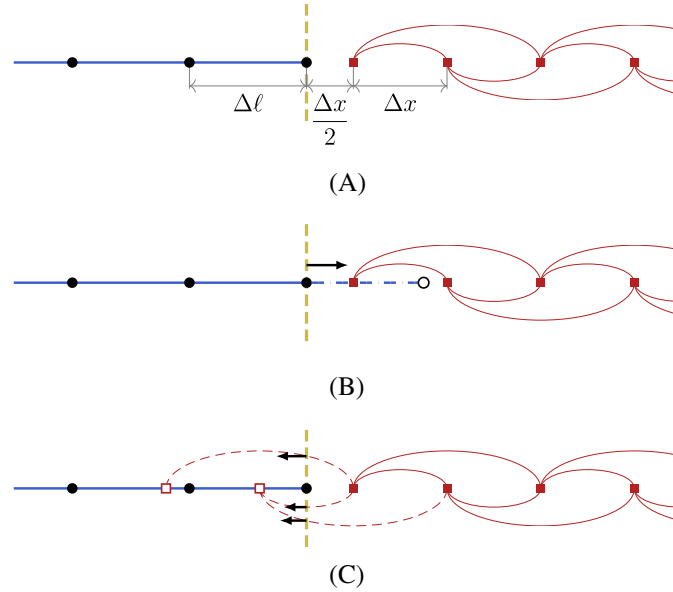
FIGURE 3 Coupling between 1D FEs and peridynamic nodes: the described interpolations ensure the continuity of the displacement field at the interface. (A) Initial geometry with real FEs (blue lines) of length $\Delta\ell$ and real PD nodes (red squares) with a uniform spacing Δx. The bonds are represented by the red line ($\delta = 2\Delta x$) and the interface between FEM and PD regions is represented by a yellow dashed line. (B) Introduction of a fictitious FE in the PD region to provide the force acting on the real FEM node at the interface. The displacement of the fictitious FEM node (empty circle) is determined by interpolation of the displacements of the real PD nodes. (C) Introduction of some fictitious PD nodes in the FEM region to provide through the fictitious bonds (red dashed lines) the forces acting on the real PD nodes near the interface. The displacements of the fictitious PD nodes (empty squares) are determined by interpolation of the displacements of the real FEM nodes.

4.2 | Interpolation of PD nodal displacements with FEM

In state-based peridynamics, each node interact with all the nodes within a distance of 2δ.[37] Therefore, the fictitious PD nodes are added within the FEs up to a distance of 2δ from the interfaces,[20] as shown in Figure 5. The displacements of these nodes can be evaluated by interpolating the displacements of the FE nodes.

Let us consider, for instance, a fictitious PD node p with a position vector $\mathbf{x}_p = \{x_p, y_p, z_p\}^\top$. Since its position is known, it is straightforward to determine within which FE node p lies. Hence, the FE shape functions N_i and the expansion functions F_τ of that element are used to compute the displacement of node p:

$$\mathbf{u}^{f\text{-}PD}(x_p, y_p, z_p) = \sum_i \sum_\tau N_i(y_p) F_\tau(x_p, z_p) \mathbf{u}_{\tau i}^{FE}, \tag{29}$$

where f-PD stands for "fictitious peridynamic" nodes. By repeating Equation (29) for each fictitious PD node, we obtain the following system of equations:

$$\mathbf{U}^{f\text{-}PD} = \mathbf{I}^{f\text{-}PD} \mathbf{U}^{FE}, \tag{30}$$

where $\mathbf{U}_f^{PD}$ is the peridynamic displacement vector of the fictitious peridynamic nodes, $\mathbf{I}^{f\text{-}PD}$ is the fictitious PD interpolation matrix and $\mathbf{U}^{FE}$ is the vector of the FE nodal unknowns. Note that the dimensions of $\mathbf{I}^{f\text{-}PD}$ are $3N^{f\text{-}PD} \times 3N^{FE}$, where $N^{f\text{-}PD}$ is the number of fictitious PD nodes and $3N^{FE}$ is the number of the FE nodal unknowns.

4.3 | Interpolation of FE nodal displacements with PD

To begin with, let us consider a simple case in which the FE sections are perpendicular to the FEs. As shown in Figure 6, the fictitious FE nodes are introduced so that the sections associated to those nodes lie over the plane of the real nodes
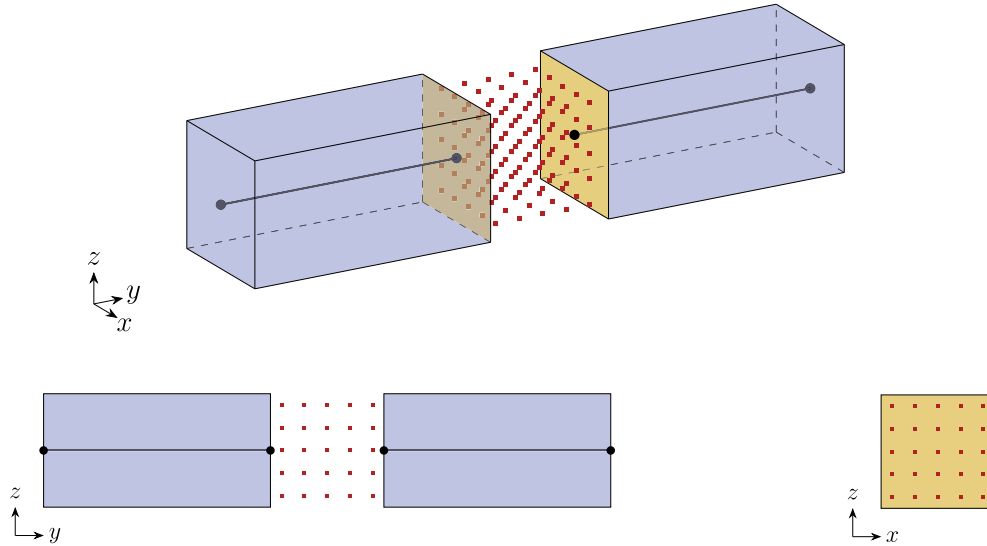
FIGURE 4 Coupling of high-order 1D FEs (blue region) with 3D peridynamic nodes (red squares). The yellow surfaces are the interfaces between FEM and peridynamic regions.
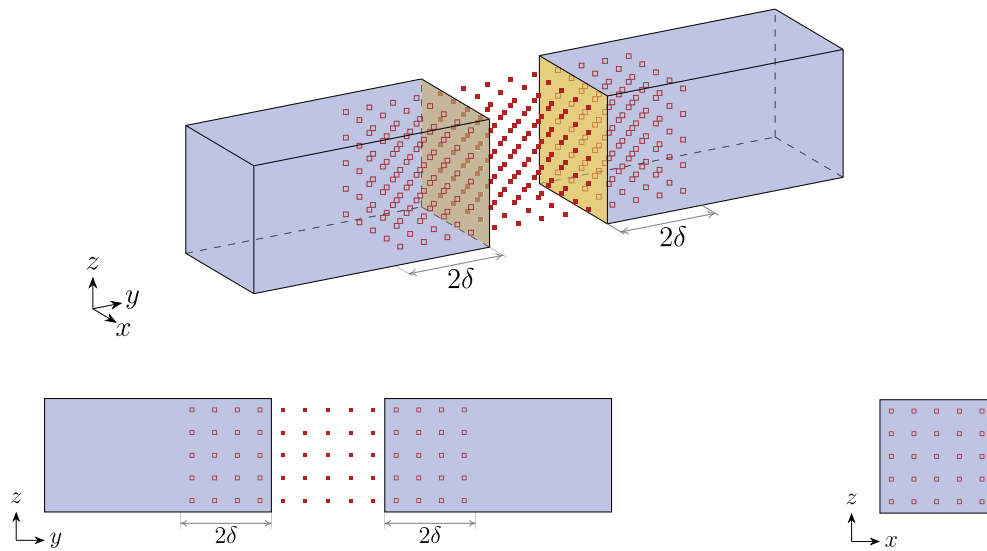
FIGURE 5 Coupling of FEs (blue region) with 3D peridynamic nodes (red solid squares): the fictitious PD nodes (red empty squares) are added within the FEs up to a distance of 2δ from the interfaces (yellow surfaces).

closest to the interface. We can write the following equation for each real PD node q that lies on the section of a fictitious FE node:

$$\mathbf{u}^{PD}(x_q, y_q, z_q) = \sum_i \sum_\tau N_i(y_q) F_\tau(x_q, z_q) \mathbf{u}_{\tau i}^{f\text{-}FE}, \tag{31}$$

where $\mathbf{u}_{\tau i}^{f\text{-}FE}$ contains the generalized degrees of freedom associated to the fictitious FE node. Equation (31) can be written in a matrix form as:

$$\mathbf{U}^{PD} = \mathbf{I}^{fs\text{-}PD} \mathbf{U}^{fs\text{-}FE}, \tag{32}$$

where $\mathbf{U}^{PD}$ is the peridynamic displacement vector, $\mathbf{I}^{fs\text{-}PD}$ is the interpolation matrix and $\mathbf{U}^{fs\text{-}FE}$ is the vector of the degrees of freedom of the section associated to a fictitious FE node.
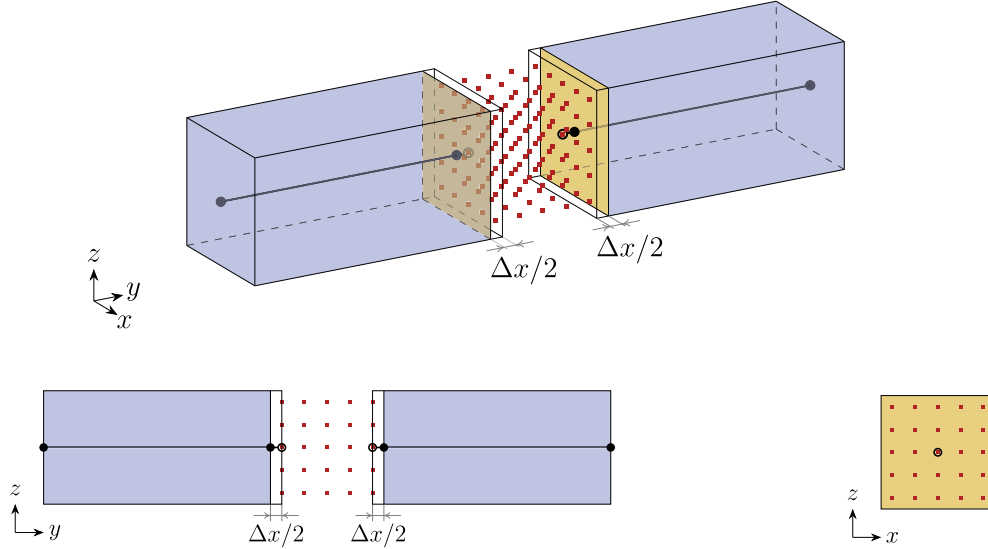
FIGURE 6 Coupling of FEs (blue region) with 3D peridynamic nodes (red squares): the fictitious FEs are added so that the sections of the fictitious FE nodes (empty circles) lie over the plane of the real PD nodes closest to the interfaces (yellow surfaces).

However, we would like to express the latter degrees of freedom ($\mathbf{U}^{fs\text{-}FE}$) as functions of the displacements of the real PD nodes ($\mathbf{U}^{PD}$) by inverting the matrix $\mathbf{I}^{fs\text{-}PD}$. Note that, in general, $\mathbf{I}^{fs\text{-}PD}$ is not a square matrix and, hence, is not invertible. Therefore, we exploit the relation of each degree of freedom of the fictitious FE node with the shape function N_i and expansion function F_τ. These functions can be used as weights to compute, for each FE degree of freedom, the weighted average of the displacements of all the real PD nodes lying on the section of the fictitious FE node:

$$\mathbf{u}_{\tau i}^{AV} = \frac{\sum_q |N_i(y_q)F_\tau(x_q,z_q)|\mathbf{u}^{PD}(x_q,y_q,z_q)}{\sum_q |N_i(y_q)F_\tau(x_q,z_q)|}, \tag{33}$$

or

$$\mathbf{U}^{AV} = \mathbf{A}\,\mathbf{U}^{PD}, \tag{34}$$

where $\mathbf{u}_{\tau i}^{AV}$ is the generic averaged displacement of the fictitious section and $\mathbf{U}^{AV}$ is the vector containing them. Note that $\mathbf{U}^{AV}$ has the same dimension of $\mathbf{U}^{fs\text{-}FE}$, so that $\left[\mathbf{A}\,\mathbf{I}^{fs\text{-}PD}\right]$ is a square matrix. This allow us to express the degrees of freedom of the fictitious FE node as functions of the displacements of the real PD nodes:

$$\begin{aligned} \mathbf{U}^{fs\text{-}FE} &= \left[\mathbf{A}\,\mathbf{I}^{fs\text{-}PD}\right]^{-1}\mathbf{U}^{AV} \\ &= \left[\mathbf{A}\,\mathbf{I}^{fs\text{-}PD}\right]^{-1}\mathbf{A}\,\mathbf{U}^{PD}. \end{aligned} \tag{35}$$

If this procedure is repeated for all the fictitious FE nodes, then the following matrix can be assembled:

$$\mathbf{U}^{f\text{-}FE} = \mathbf{I}^{f\text{-}FE}\mathbf{U}^{PD}, \tag{36}$$

where $\mathbf{U}^{f\text{-}FE}$ is the vector of the degrees of freedom of the fictitious FE nodes and $\mathbf{I}^{f\text{-}FE}$ is the fictitious FE interpolation matrix. Note that the dimensions of $\mathbf{I}^{f\text{-}FE}$ are $3N^{f\text{-}FE} \times 3N^{PD}$, where $3N^{f\text{-}FE}$ is the number of the FE nodal unknowns and N^{PD} is the number of real PD nodes.

> *Remark* 1. There might be the case in which a fictitious CUF node is associated to more-than-one section, as for instance shown in Figure 7. Let us call n the number of sections to which the CUF node belongs. In this case, the procedure explained above should be repeated n times, and the row of $\mathbf{I}^{f\text{-}FE}$ should be divided by n. In this way, the interpolation of the FE node is the average of the contributions of the n sections.
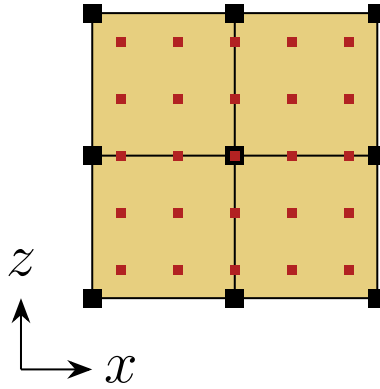
FIGURE 7 Example of a FE node with multiple FE sections in which some fictitious FE nodes belong to more-than-one section and some real PD nodes lie on more-than-one section.
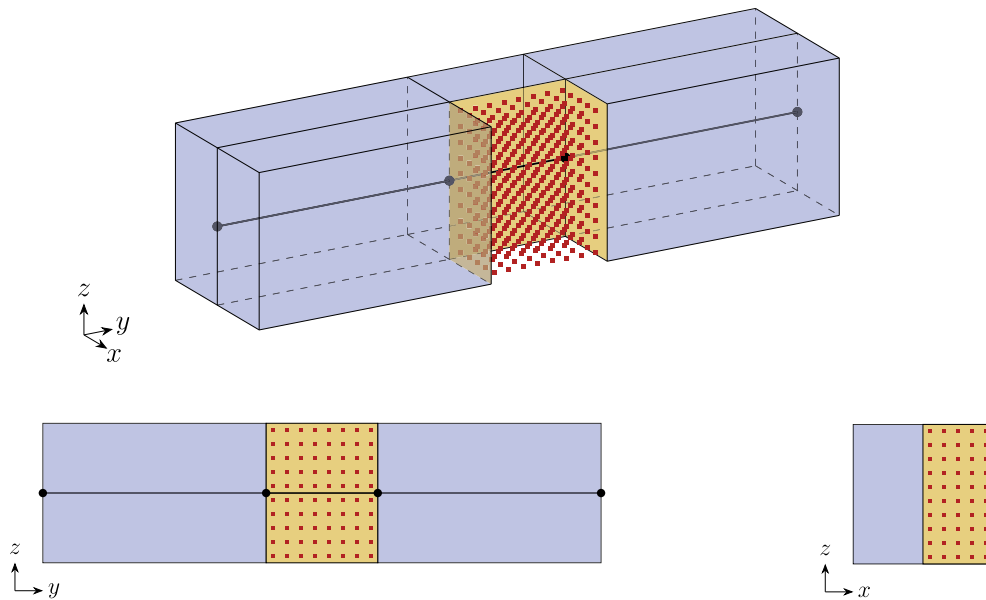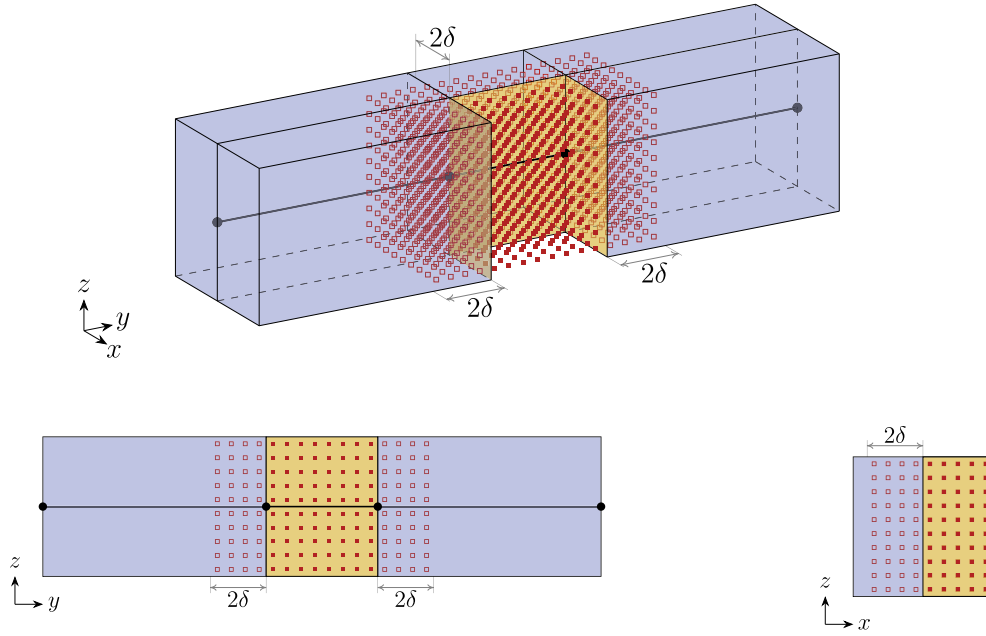

FIGURE 8 Coupling of high-order 1D FEs (blue region) with 3D peridynamic nodes (red squares) when one of the interfaces (yellow surfaces) is parallel to the axis of the bar.

Remark 2. There might be the case in which some real PD nodes lie in more-than-one fictitious FE section, as for instance shown in Figure 7. In this case, the PD nodes are involved in the interpolation of each CUF section they lie on.

4.4 | Interfaces parallel to FEs

Let us consider another example in which there is an interface that is parallel to y axis, that is, the axis of the bar, as in Figure 8. It is straightforward to generalize this example to more complex cases in which there are interfaces perpendicular to both x and z axes. Similarly to what exposed in Section 4.2, the fictitious PD nodes are introduced within the FEs in such a way to surround the interfaces with a PD layer with thickness 2δ, as shown in Figure 9. Equation (29) is still valid and can be used to assemble the fictitious PD interpolation matrix $\mathbf{I}^{f\text{-}PD}$.

On the other hand, the fictitious FE sections are added in the PD region so that they lie on the closest plane of real PD nodes, as shown in Figure 10. Note that a new kind of fictitious FEs is generated by this geometry: close to the edge between the interfaces there are some fictitious FEs with just one edge lying on a row of real PD nodes. The other edges

FIGURE 9 Coupling of FEs (blue region) with 3D peridynamic nodes (red solid squares): the fictitious PD nodes (red empty squares) are added within the FEs up to a distance of 2δ from all the interfaces (yellow surfaces), even the interfaces parallel to the axis of the bar.

of that kind of elements lie on the external surface of real FEs. This means that, for these new elements, there are no sections as the ones used in Section 4.3 to interpolate the displacements of the fictitious FE nodes.

In this case, the displacements of the fictitious FE nodes lying on the row of PD nodes are interpolated thanks to the two fictitious FE sections as explained in Section 4.3. Note that the row of PD nodes is involved in both the interpolations of the two fictitious FE sections (see Remark 2). Analogously, since the fictitious FE nodes lying on that edge are "shared" between the two fictitious FE sections, the displacements of these nodes are the averages of the interpolations of the two sections (see Remark 1). The fictitious FE nodes of the remaining edges, lying on the external surfaces of real FEs, are simply interpolated via the FE shape functions N_i and the expansion functions F_τ of those elements:

$$\mathbf{u}^{fe\text{-}FE}(x_p, y_p, z_p) = \sum_i \sum_\tau N_i(y_p) F_\tau(x_p, z_p) \mathbf{u}_{\tau i}^{FE}, \tag{37}$$

where $\mathbf{u}^{fe\text{-}FE}$ is the vector of the degrees of freedom of the fictitious FE nodes on one of these edges. Equation (37) is employed during the assembling of the fictitious FE interpolation matrix $\mathbf{I}^{f\text{-}FE}$.

4.5 | 3D coupling of FEs and PD nodes

In this section, we aim at assembling the stiffness matrix of the complete system of (both FE and PD) equations. We assemble the global FE stiffness matrix $\mathbf{K}^{gl-FE}$ as explained in Section 3 by considering both real and fictitious elements. The real FE stiffness matrix $\mathbf{K}^{FE}$ is retrieved by eliminating all the rows and columns of $\mathbf{K}^{gl-FE}$ corresponding to fictitious FE degrees of freedom. On the other hand, the fictitious FE stiffness matrix $\mathbf{K}^{f-FE}$ is obtained by eliminating the rows corresponding to fictitious FE degrees of freedom and the columns corresponding to real FE degrees of freedom. Note that the rows of the fictitious degrees of freedom are not utilized because they correspond to the fictitious FE forces. The fictitious FE nodes indeed lie in the peridynamic region and do not "feel" any FE force, as explained in Section 4.1.

Similarly, as explained in Section 2, we assemble the global PD stiffness matrix $\mathbf{K}^{gl-PD}$ by considering both real and fictitious PD nodes. Since the fictitious PD nodes lie within FEs, there are no fictitious PD forces applied to those nodes. Therefore, the rows of $\mathbf{K}^{gl-PD}$ are eliminated. We obtain the real PD stiffness matrix $\mathbf{K}^{PD}$ and the fictitious PD stiffness matrix $\mathbf{K}^{f-PD}$ by eliminating the columns corresponding to the fictitious and real degrees of freedom, respectively.
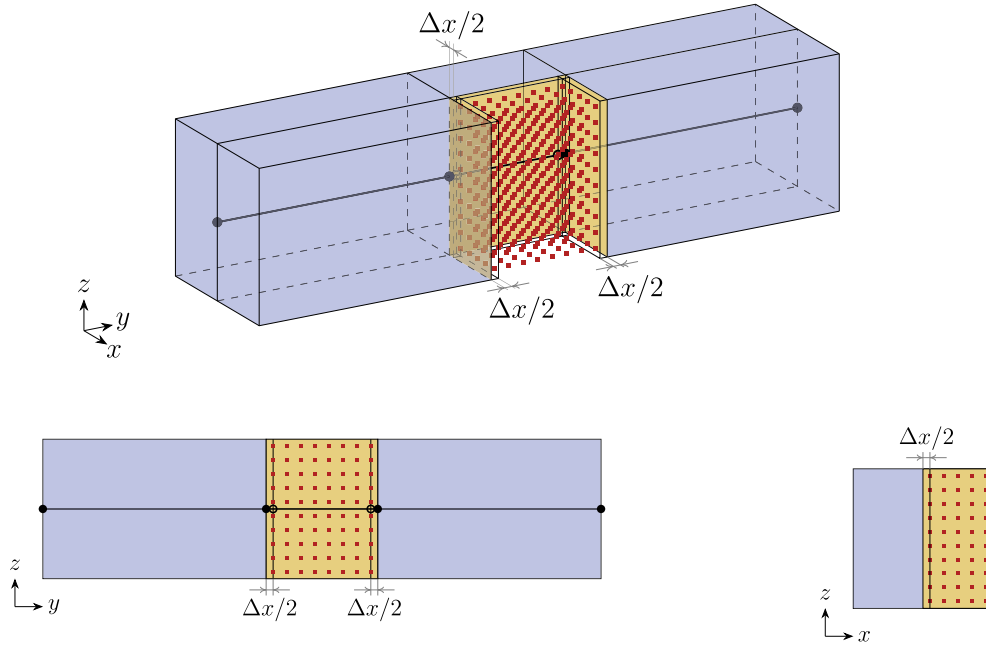
FIGURE 10   Coupling of FEs (blue region) with 3D peridynamic nodes (red squares): the fictitious FEs are added so that the fictitious sections lie over the plane of the real PD nodes closest to the interfaces (yellow surfaces). Note that a new type of elements appears near the edges between the interfaces.

Thus, the system of equations can be written in the following matrix form:

$$
\begin{bmatrix} \mathbf{K}^{FE} & \mathbf{K}^{f-FE}\,\mathbf{I}^{f-FE} \\ \mathbf{K}^{f-PD}\,\mathbf{I}^{f-PD} & \mathbf{K}^{PD} \end{bmatrix} \begin{bmatrix} \mathbf{U}^{FE} \\ \mathbf{U}^{PD} \end{bmatrix} = \begin{bmatrix} \mathbf{F}^{FE} \\ \mathbf{F}^{PD} \end{bmatrix},
\tag{38}
$$

or

$$
\mathbf{KU} = \mathbf{F},
\tag{39}
$$

where $\mathbf{K}$ is the stiffness matrix of the entire system, $\mathbf{U}$ is the displacement vector and $\mathbf{F}$ is the force vector.

5 | NUMERICAL EXAMPLES

In the following Section, we will analyze various numerical examples to verify the accuracy of the proposed coupling method. We will compare these results with full FEM solutions, even if the different formulations of peridynamics and classical continuum mechanics lead to a discrepancy in the results between the two theories.[26] Moreover, no corrections to the surface effect has been applied for the external surfaces of the PD regions (the surfaces that do not correspond to interfaces with FEM regions).[5-8] As one will see hereinafter, these sources of error affect only slightly the accuracy of the numerical results.

5.1 | Isotropic bar

The first case study is a 3D isotropic bar subjected to uniaxial traction. Geometry, boundary conditions, and mesh information are highlighted in Figure 11. The bar has a squared cross-section, and each side is 10 mm long, whereas the longitudinal length of the beam is equal to 100 mm. The material is isotropic and homogeneous, with an elastic modulus $E = 10$ GPa and Poisson's ratio $\nu = 0.2$. The central portion of the isotropic bar is modeled with a 3D peridynamics
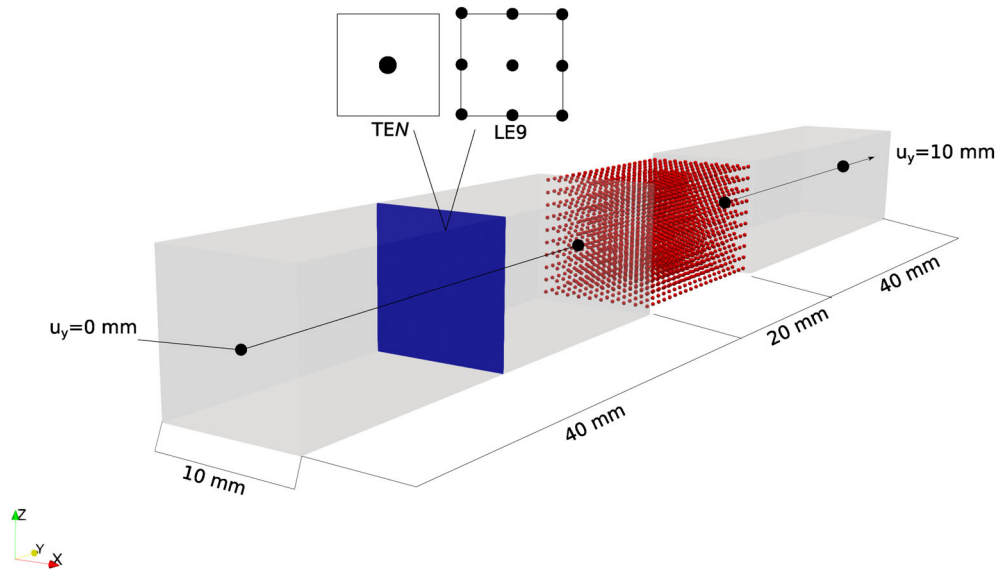
**FIGURE 11** Geometrical and modeling features of the investigated beam.
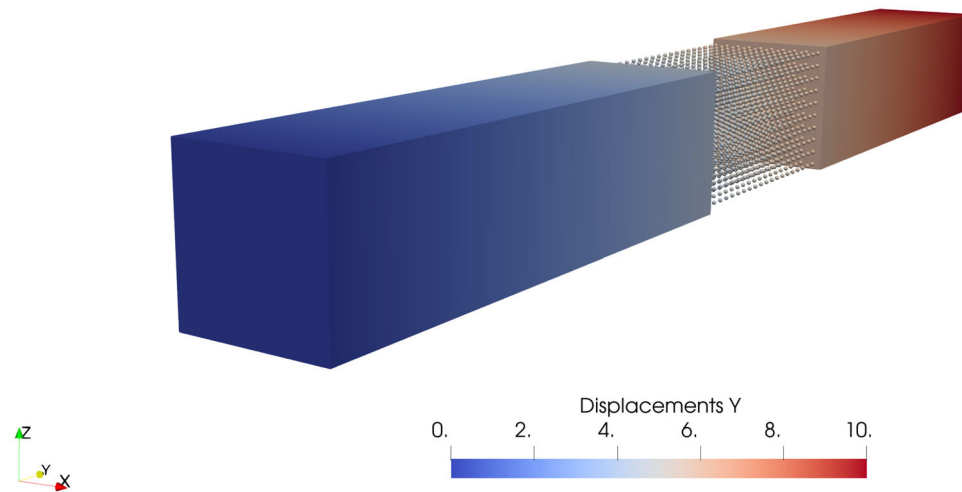
FIGURE 12 Deformed configuration under uniaxial traction. In this numerical case, the 1D finite elements adopt a quadratic (L9) kinematics.

grid. A grid spacing of $\Delta x = 1$ mm and an m-ratio equal to 3 is adopted, resulting in a horizon radius $\delta = 3$ mm. The remaining portions of the bar are described by linear two-nodes finite elements (B2), one for each region. Hence, by using CUF, the kinematics associated with the finite elements goes from classical beam models to high-order LE. More specifically, Taylor expansion of different orders N (TEN) are adopted. Thus, for instance, the notation TE1 refers to the use of first-order polynomials as expansion function. Nine-node quadratic Lagrange elements (LE9) are also used in the present case. Three-dimensional peridynamics has already been coupled with CUF before.[22] The same bar has been here investigated. However, a bond-based formulation has been adopted in that case, leading to a constrained value of Poisson ratio $\nu = 0.25$. The extension to a state-based formulation eliminates this constraint. Moreover, in Reference 22 the coupling method is based on the application of Lagrange multipliers at the FEM-PD interface. The results from this coupling approach showed to be in good accordance with the full FEM solution. Nevertheless, some discrepancies at the interface have been detected. The present work's objective is to reduce these numerical errors at FEM-PD domain interfaces.

A first result is shown in Figure 12. The deformed shape of the bar under uniaxial displacement is represented. In this particular case, a single LE9 element has been adopted for the cross-section discretization. Figure 13
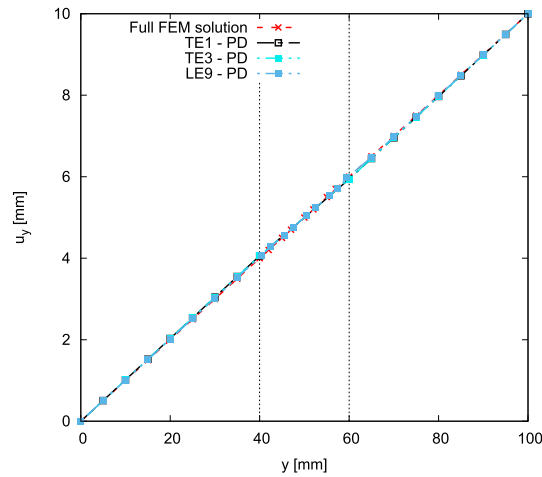
**FIGURE 13** Effect of different 1D-CUF models for FEM regions on the axial displacement of the beam.

shows the consistency of the solutions when 3D PD is coupled with different FE models. Indeed, the longitudinal displacement evaluated in the central point of the section along the bar length is not affected by the cross-section discretization. A comparison between the aforementioned method and the present one is displayed in Figure 14. This figure shows the presence of some distortions for displacements at interface regions when the Lagrange multipliers method is adopted (see Figure 14B). Figure 14C shows that these discrepancies are nearly eliminated when the proposed model is adopted, especially at the interfaces. In fact, a relative error with respect to the full FEM solution greater than 5% is computed at the FEM-PD interfaces, when the Lagrange multipliers method is adopted. On the other hand, the error is significantly reduced with the present coupling technique, leading to a maximum relative error of 0.69%.

5.2 | C-shaped section beam under bending and torsion

The second analysis case is a C-section beam subjected to bending and torsion. The information about dimensions, boundary conditions, and modeling features are detailed in Figure 15. The entire beam is made of the same isotropic material, with elastic modulus $E = 200$ GPa and Poisson ratio $\nu = 0.2$. The main objective of this case study is to highlight the 3D nature of the proposed coupling model. In fact, high-order LE elements are required to accurately describe the beam behavior under both bending and torsion. It has been widely demonstrated that classical low-order beam theories have significant difficulties in reproducing these 3D phenomena.

In this case study, the axial FEM discretization consists of 10 four-node cubic elements (B4). The 3D PD region is not adopted for modeling the whole cross-section, as in the previous case. Instead, the PD region is here embedded into the finite element domain itself. This solution is obtained by varying the cross-section of the 1D FEs along the axial direction; it is represented by a disconnected region wherever PD is employed, that is, $490 \leq y \leq 510$ mm (see Figure 15). A grid spacing of $\Delta x = 1$ mm and horizon radius $\delta = 3$ mm is chosen. In Figure 16, the deformed shape of the C-section beam for both full FEM (Figure 16A) and coupled PD-FEM model (Figure 16B) are shown. Furthermore, a close detail of the deformed state is displayed in Figure 17. One can notice that the three-dimensional PD domain is perfectly consistent with the FEM regions.

These considerations support the choice of using high-order Lagrange elements capable of reproducing 3D-like phenomena. Table 1 compares the vertical displacements at points A and B (see Figure 15) from the improved coupled FE-PD model with those from reference solutions, obtained by using CUF-based TE and LE refined models. Displacements in two different points are evaluated in order to highlight further the capability of the refined CUF models to capture both bending and torsional behavior of the investigated beam. A first remark can be identified in the difficulty of low-order theories in computing the correct displacements in both investigated points. The model adopting LE9 elements for cross-section discretization reaches an optimal solution, as shown in recent works (i.e., Reference 24). Moreover, the
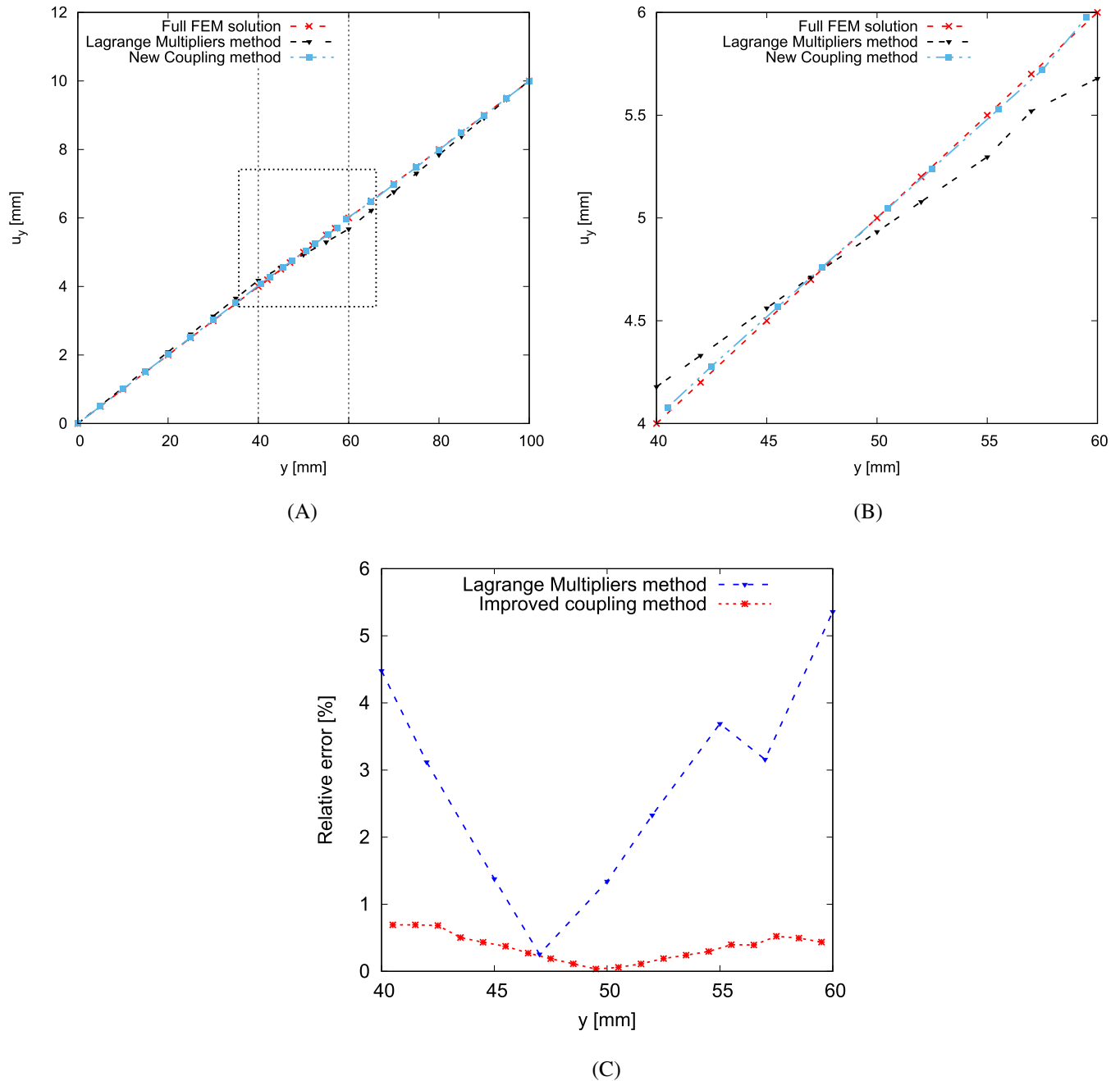
FIGURE 14 Axial displacement of the bar subjected to traction along (A) the entire length and (B) the perydinamic region. FE-PD interfaces are subjected to distortions when the Lagrange multipliers coupling approach is adopted. These distortions are eliminated when the improved coupling method is applied. A comparison of the errors retrieved with both methods with respect to the full FEM solution is presented in (C).

present improved coupling model leads to transverse displacements comparable to those obtained with fully refined models, with an error of 1 % and 2 % detected in points A and B, respectively.

Finally, the vertical displacement along the beam span is given in Figure 18. The green line in Figure 15 indicates the followed path. Results from the present coupling model are compared with a full FEM solution. The displacement evolution along the beam span is correctly reproduced by the FEM-PD model. Furthermore, it should be underlined the capability of the improving coupling solution in avoiding any distortions at domain interfaces. In fact, a smooth transition between FEM (red dots) and PD (green dots) displacements is retrieved. The residual errors that are still noticeable in Figure 18 are due to the different (local and nonlocal) solutions of peridynamics and CUF when the displacement field
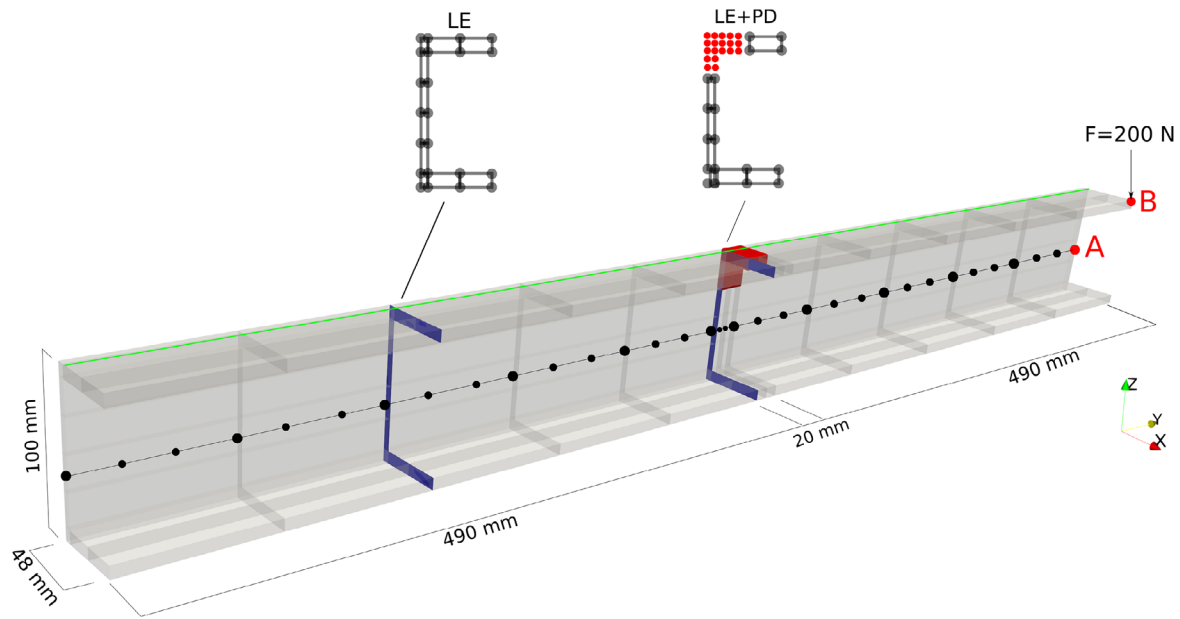
FIGURE 15   Geometrical and modeling features of C-shaped section beam subjected to bending and torsion.
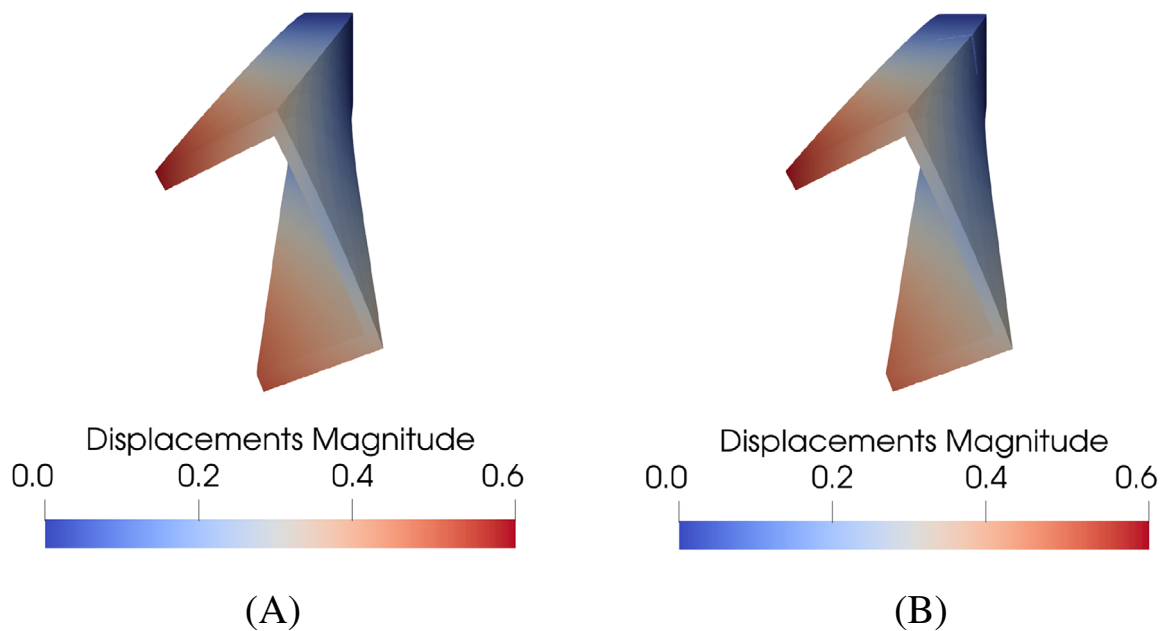

FIGURE 16   Deformed configuration of the C-section beam for (A) full FEM and (B) FE-PD coupled model.

is a superlinear function.[26] Moreover, the lack of corrections for the peridynamic surface effect may further increase the differences between the results obtained with the full FEM approach and the CUF-PD coupling. The simplest way to reduce these residual errors is decreasing the horizon size.

5.3 | Stiffened panel

A stiffened panel is investigated as final example to underline the ability of the proposed method to introduce PD domains in complex structures. Figure 19 summarizes geometric and modeling features. The material properties are the same
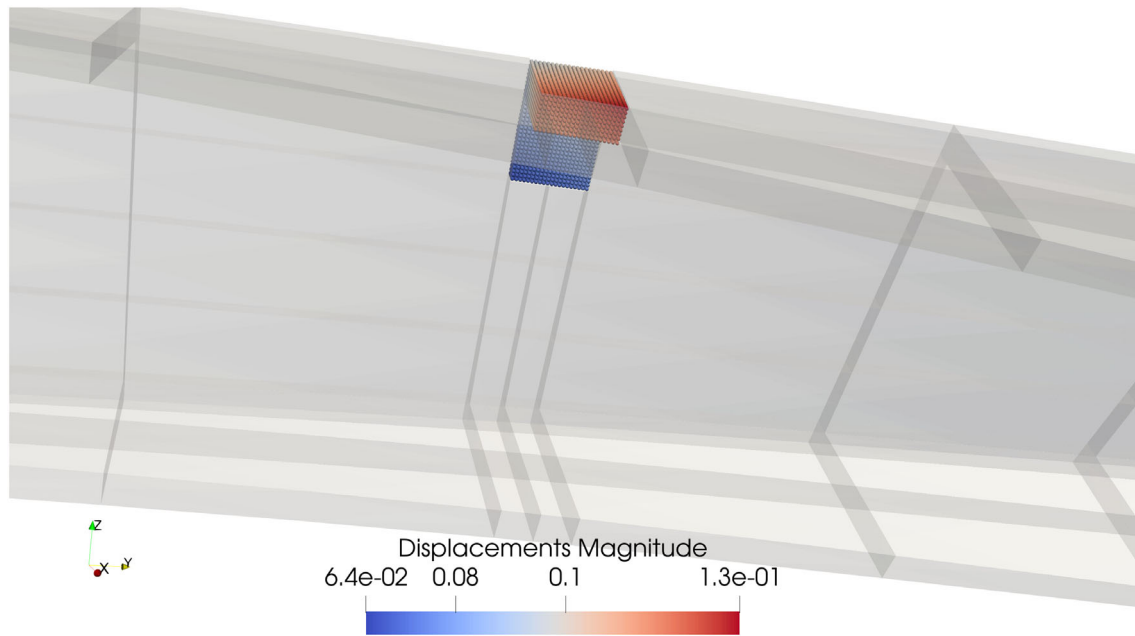
FIGURE 17 Close view of the deformed PD zone for the investigated beam. A clear consistency between the two formulation is shown.

TABLE 1 Transverse displacements in middle point of the free-end section (Point A) and at the loading point (Point B).

Model	FE dof's	PD dof's	$-u_z$ [mm] Point A	$-u_z$ [mm] Point B
TE1	333	-	0.1713	0.1732
TE4	1665	-	0.1959	0.2658
TE8	4995	-	0.2646	0.5252
L9	9657	-	0.2403	0.5436
L9-PD	9432	20,040	0.2344	0.5337

adopted in the first numerical case. The structure is composed of two stringers and one panel, which are independently modeled with high-order four-node beam elements in a component-wise manner.[38]

The main novelty introduced with this numerical case is the possibility of investigating a structure with two distinct peridynamics domains. In fact, two different square regions, one for each stringer, are modeled through 3D peridynamics. The PD domain is discretized in a meshless manner with a grid spacing of $\Delta x = 1$ mm and horizon radius $\delta = 3$ mm.
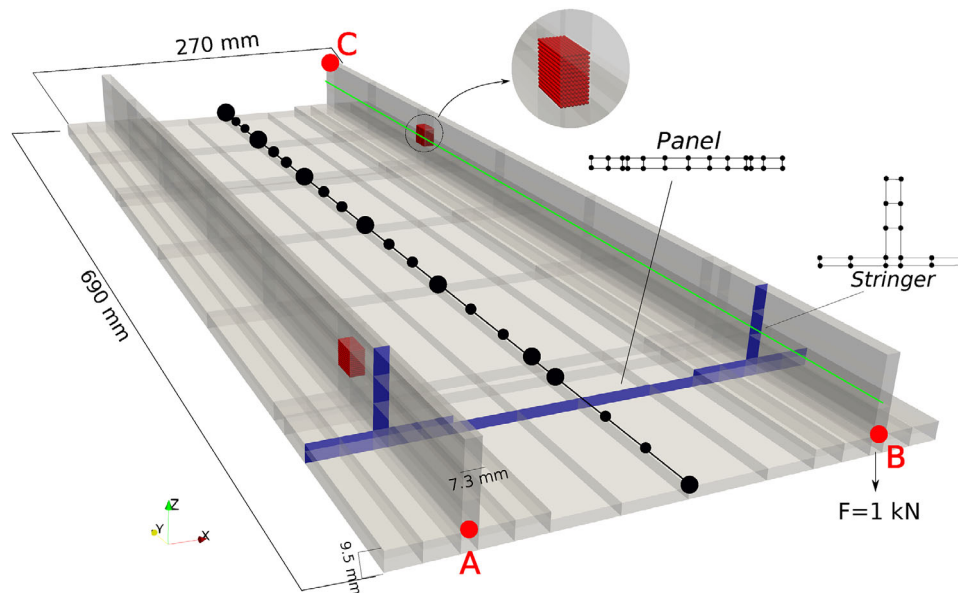
Table 2 displays the vertical displacement and the value of longitudinal stress σ_{yy} in some characteristic points (see Figure 19) for the present coupled model and for reference solutions obtained through full FEM analysis. These results underline once again the capability of the proposed coupling model in accurately reproducing three-dimensional phenomena.

Furthermore, the accurate prediction of the axial stress in point C of the structure should be highlighted. Figure 20 also shows the complete axial stress state in the structure for a FEM solution (Figure 20A) and the coupled model (Figure 20B). It is important to remark here that the PD domain embedded into the structure does not affect the stress state, opening the possibility of using FEM-PD coupled models for fracture mechanics problems (see Reference 36).

Vertical displacement along the green line in Figure 19 is displayed in Figure 21. The solution from a full FEM analysis is depicted with a solid blue line, while red and green dots represent displacements in FEM and PD domains, respectively. The coupled model completely matches the FEM solution along the beam span and across the perydinamic region without any sign of distortion in both FE-PD interfaces. Similarly to the previous case presented in Section 5.2, the residual errors are due to the different formulations of peridynamics and CUF theories.
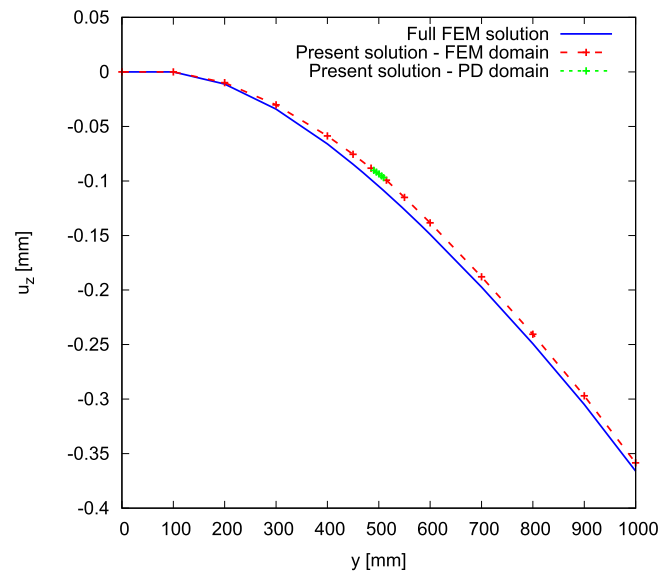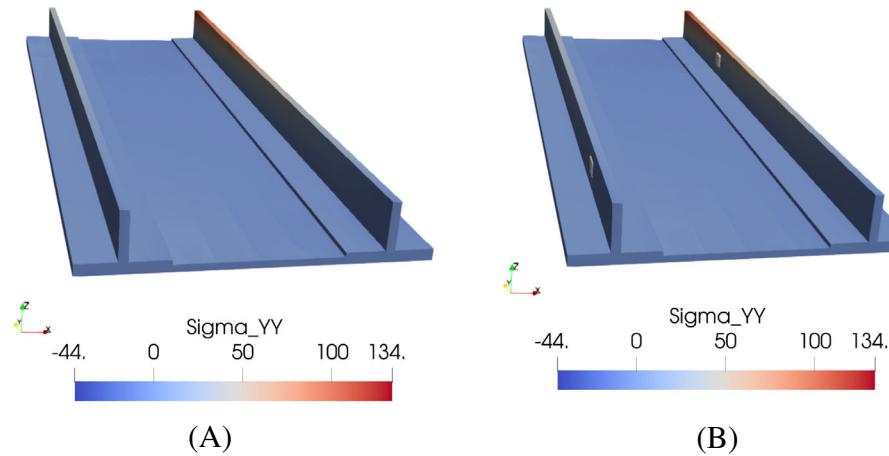
FIGURE 18 Vertical displacement of the C-section beam along the beam span (green line in Figure 15). A full FEM solution (solid blue line) is used as reference, while red and green dots represent the displacement in FEM and PD domains, respectively.


FIGURE 19 Geometrical and modeling features of the investigated reinforced panel. Two distinct peridynamic regions are introduced, one for each stringer.

TABLE 2 Vertical displacements and axial stress σ_{yy} are evaluated in some characteristic points of the structure for reference solutions and present FE-PD coupled model.

Model	FE dof's	PD dof's	$-u_z$ [mm] @Point A	$-u_z$ [mm] @Point B	σ_{yy} [MPa] @ Point C
TE1	225	-	29.532	29.368	71.274
TE4	1125	-	31.471	27.513	89.505
TE8	3378	-	40.765	18.396	114.42
L9	10659	-	44.942	14.153	126.916
L9-PD	10641	15,480	45.346	14.719	126.847

FIGURE 20 Distribution of longitudinal stress σ_{yy} in the reinforced panel for a full FEM analysis (A) and for a coupled FE-PD model (B).
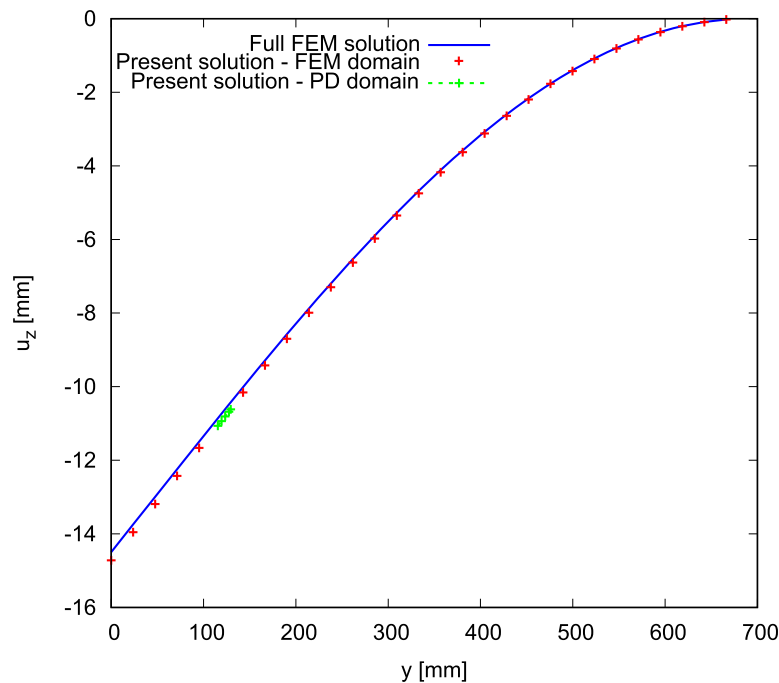
FIGURE 21 Vertical displacements along the structure span, following the green line in Figure 19. A full FEM solution (solid blue line) is used as reference, while red and green dots represent the displacement in FEM and PD domains, respectively.

6 | CONCLUSIONS

In this research, a method for the coupling of three-dimensional (3D) peridynamics grids and one-dimensional (1D) refined finite elements (FEs) based on Carrera Unified Formulation (CUF) is proposed. The advantages of CUF are exploited to obtain 3D solutions with a significant reduction in computational demand. In fact, CUF allows coupling 3D peridynamics domains with 1D finite elements of any order. By adopting high-order 1D models, full 3D solutions are retrieved, even when peridynamics is introduced in multiple regions of the investigated structure. The proposed technique has proven to be general and capable of greatly reducing any numerical inaccuracies at the interfaces between the two domains. Furthermore, the use of the state-based peridynamics (instead of the bond-based peridynamics) allows to remove the limitation of modeling only materials with a Poisson's ratio equal to 0.25. The present coupling method is

based on the continuity of the displacement field in a nonlocal region near the interfaces. The employed coupled models show a very low computational cost when compared with full 3D approaches while maintaining a great degree of accuracy. The effectiveness and efficiency of the present coupling strategy are proven on classical beams and thin-walled structures of aerospace interest.

CONFLICT OF INTEREST STATEMENT
The authors declare that they have no known competing financial interests or personal relationships that could have appeared to influence the work reported in this article.

DATA AVAILABILITY STATEMENT
The data that support the findings of this study are available on request from the corresponding author.

ORCID
M. Enea https://orcid.org/0000-0002-6622-3763

REFERENCES
1. Silling SA. Reformulation of elasticity theory for discontinuities and long-range forces. *J Mech Phys Solids*. 2000;48(1):175-209. doi:10.1016/S0022-5096(99)00029-0
2. Silling SA, Epton M, Weckner O, Xu J, Askari E. Peridynamic states and constitutive modeling. *J Elast*. 2007;88(2):151-184. doi:10.1007/s10659-007-9125-1
3. Ni T, Zaccariotto M, Zhu Q, Galvanetto U. Static solution of crack propagation problems in peridynamics. *Comput Methods Appl Mech Eng*. 2019;346:126-151. doi:10.1016/j.cma.2018.11.028
4. Ha Y, Bobaru F. Characteristics of dynamic brittle fracture captured with peridynamics. *Eng Fract Mech*. 2011;78(6):1156-1168. doi:10.1016/j.engfracmech.2010.11.020
5. Le QV, Bobaru F. Surface corrections for peridynamic models in elasticity and fracture. *Comput Mech*. 2018;61(4):499-518. doi:10.1007/s00466-017-1469-1
6. Scabbia F, Zaccariotto M, Galvanetto U. A novel and effective way to impose boundary conditions and to mitigate the surface effect in state-based peridynamics. *Int J Numer Methods Eng*. 2021;122(20):5773-5811. doi:10.1002/nme.6773
7. Scabbia F, Zaccariotto M, Galvanetto U. A new method based on Taylor expansion and nearest-node strategy to impose Dirichlet and Neumann boundary conditions in ordinary state-based peridynamics. *Comput Mech*. 2022a;70:1-27. doi:10.1007/s00466-022-02153-2
8. Scabbia F, Zaccariotto M, Galvanetto U. A new surface node method to accurately model the mechanical behavior of the boundary in 3D state-based Peridynamics. *J Peridyn Nonlocal Model*. 2023;1-35. doi:10.1007/s42102-022-00094-1
9. Kilic B, Madenci E. Coupling of peridynamic theory and the finite element method. *J Mech Mater Struct*. 2010;5(5):707-733. doi:10.1007/978-1-4614-8465-3_11
10. Lubineau G, Azdoud Y, Han F, Rey C, Askari A. A morphing strategy to couple non-local to local continuum mechanics. *J Mech Phys Solids*. 2012;60(6):1088-1102. doi:10.1016/j.jmps.2012.02.009
11. Han F, Lubineau G. Coupling of nonlocal and local continuum models by the arlequin approach. *Int J Numer Methods Eng*. 2012;89(6):671-685. doi:10.1002/nme.3255
12. Seleson P, Beneddine S, Prudhomme S. A force-based coupling scheme for peridynamics and classical elasticity. *Comput Mater Sci*. 2013;66:34-49. doi:10.1016/j.commatsci.2012.05.016
13. Seleson P, Ha Y, Beneddine S. Concurrent coupling of bond-based peridynamics and the navier equation of classical elasticity by blending. *Int J Multiscale Comput Eng*. 2015;13(2):91-113. doi:10.1615/IntJMultCompEng.2014011338
14. Silling S, Littlewood D, Seleson P. Variable horizon in a peridynamic medium. *J Mech Mater Struct*. 2015;10(5):591-612. doi:10.2140/jomms.2015.10.591
15. Sun W, Fish J, Zhang G. Superposition of non-ordinary state-based peridynamics and finite element method for material failure simulations. *Meccanica*. 2019;55:681-699. doi:10.1007/s11012-019-01098-w
16. Galvanetto U, Mudric T, Shojaei A, Zaccariotto M. An effective way to couple FEM meshes and Peridynamics grids for the solution of static equilibrium problems. *Mech Res Commun*. 2016;76:41-47. doi:10.1016/j.mechrescom.2016.06.006
17. Zaccariotto M, Mudric T, Tomasi D, Shojaei A, Galvanetto U. Coupling of FEM meshes with Peridynamic grids. *Comput Methods Appl Mech Eng*. 2018;330:471-497. doi:10.1016/j.cma.2017.11.011
18. Shojaei A, Mudric T, Zaccariotto M, Galvanetto U. A coupled meshless finite point/Peridynamic method for 2D dynamic fracture analysis. *Int J Mech Sci*. 2016;119:419-431. doi:10.1016/j.ijmecsci.2016.11.003

19. Zaccariotto M, Tomasi D, Galvanetto U. An enhanced coupling of PD grids to FE meshes. *Mech Res Commun*. 2017;84:125-135. doi:10.1016/j.mechrescom.2017.06.014

20. Ni T, Zaccariotto M, Zhu QZ, Galvanetto U. Coupling of FEM and ordinary state-based peridynamics for brittle failure analysis in 3D. *Mech Adv Mater Struct*. 2021;28(9):875-890. doi:10.1080/15376494.2019.1602237

21. Ongaro G, Bertani R, Galvanetto U, Pontefisso A, Zaccariotto M. A multiscale peridynamic framework for modelling mechanical properties of polymer-based nanocomposites. *Eng Fract Mech*. 2022;274:108751. doi:10.1016/j.engfracmech.2022.108751

22. Pagani A, Carrera E. Coupling three-dimensional peridynamics and high-order one-dimensional finite elements based on local elasticity for the linear static analysis of solid beams and thin-walled reinforced structures. *Int J Numer Methods Eng*. 2020;121(22):5066-5081. doi:10.1002/nme.6510

23. Carrera E, Pagani A, Petrolo M. Use of Lagrange multipliers to combine 1D variable kinematic finite elements. *Comput Struct*. 2013a;129:194-206. doi:10.1016/j.compstruc.2013.07.005

24. Carrera E, Pagani A. Analysis of reinforced and thin-walled structures by multi-line refined 1D/beam models. *Int J Mech Sci*. 2013a;75:278-287. doi:10.1016/j.ijmecsci.2013.07.010

25. Carrera E, Pagani A. Multi-line enhanced beam model for the analysis of laminated composite structures. *Compos Part B Eng*. 2014;57:112-119. doi:10.1016/j.compositesb.2013.09.046

26. Ongaro G, Seleson P, Galvanetto U, Ni T, Zaccariotto M. Overall equilibrium in the coupling of peridynamics and classical continuum mechanics. *Comput Methods Appl Mech Eng*. 2021;381:113515. doi:10.1016/j.cma.2020.113515

27. Silling SA, Askari E. A meshfree method based on the peridynamic model of solid mechanics. *Comput Struct*. 2005;83(17-18):1526-1535. doi:10.1016/j.compstruc.2004.11.026

28. Seleson P. Improved one-point quadrature algorithms for two-dimensional peridynamic models based on analytical calculations. *Comput Methods Appl Mech Eng*. 2014;282:184-217. doi:10.1016/j.cma.2014.06.016

29. Scabbia F, Zaccariotto M, Galvanetto U. Accurate computation of partial volumes in 3D peridynamics. *Eng Comput*. 2022b;39:1-33. doi:10.1007/s00366-022-01725-3

30. Bobaru F, Ha YD. Adaptive refinement and multiscale modeling in 2D peridynamics. *J Multiscale Comput Eng*. 2011;9(6):635-659. https://digitalcommons.unl.edu/mechengfacpub/98

31. Seleson P, Littlewood DJ. Convergence studies in meshfree peridynamic simulations. *Comput Math Appl*. 2016;71(11):2432-2448. doi:10.1016/j.camwa.2015.12.021

32. Parks ML, Plimpton SJ, Lehoucq RB, Silling SA. *Peridynamics with LAMMPS: a User Guide. Technical Report*. Sandia National Laboratories; 2008.

33. Carrera E, Cinefra M, Petrolo M, Zappino E. *Finite Element Analysis of Structures through Unified Formulation*. John Wiley & Sons; 2014.

34. Pagani A, Enea M. Displacement and strain data-driven damage detection in multi-component and heterogeneous composite structures. *Mech Adv Mater Struct*. 2022;1-16. doi:10.1080/15376494.2022.2149907

35. Refat M, Zappino E, Sánchez-Majano AR, Pagani A. Dynamic characterization of 3D printed lightweight structures. *Adv Aircraft Spacecraft Sci*. 2022;9(4):301-318. doi:10.12989/aas.2022.9.4.301

36. Pagani A, Enea M, Carrera E. Quasi-static fracture analysis by coupled three-dimensional peridynamics and high order one-dimensional finite elements based on local elasticity. *Int J Numer Methods Eng*. 2022;123(4):1098-1113. doi:10.1002/nme.6890

37. Silling SA. Linearized theory of peridynamic states. *J Elast*. 2010;99(1):85-111. doi:10.1007/s10659-009-9234-0

38. Carrera E, Pagani A, Petrolo M. Classical, refined, and component-wise analysis of reinforced-shell wing structures. *AIAA J*. 2013b;51(5):1255-1268. doi:10.2514/1.J052331